Gravity modeling of the Alpine lithosphere affected by magmatism based on seismic tomography

Davide Tadiello[1], Carla Braitenberg[1]

[1]Department of Mathematics and Geosciences, University of Trieste

Correspondence to: Davide Tadiello (tadiellodavide@gmail.com), Carla Braitenberg (berg@units.it)

Key words: Gravity modelling, 3D density modes, Magmatic underplating, Seismic tomography, AlpsArray

Abstract. The Southern Alpine regions have been affected by several magmatic and volcanic events between the Paleozoic and the Tertiary. This activity has undoubtedly had an important effect on the density distribution and structural setting at lithosphere scale. Here the gravity field is used to create a 3D lithosphere density model on the base of a high-resolution seismic tomography model. The results of the gravity modelling demonstrate a highly complex density distribution in good agreement with the different geological domains of the Alpine area represented by the European plate, the Adriatic plate and the Tyrrhenian basin. The Adriatic derived terrains (Southalpine and Austrolpine) of the Alps are typically denser (2850 kg m^{-3}), whilst the Alpine zone composed by European terrains provenance (Helvetic and Tauern window) presents lower density values (2750 kg m^{-3}). Inside the Southalpine, south of the Dolomites, a well-known positive gravity anomaly is present and one of the aims of this work is to investigate the source of this anomaly that has not yet been explained. The modelled density suggests that the anomaly is related to two different sources, the first involves the middle-crust below the gravity anomaly and is represented by localized mushroom-shaped bodies interpreted as a magmatic intrusion, while a second wider density anomaly affects the lower crust of the Southern Alpine realm and could correspond to a mafic and ultramafic magmatic underplating (gabbros and related cumulates) developed during Paleozoic extension.

1 Introduction

In a recent work, Kästle et al. (2018) made/published a 3D seismic tomography of the lithosphere in the Alps, which forms an ideal basis for a 3D density modeling of the globally available gravity field derived from the integration of satellite and terrestrial data. The 3D inversion of gravity data is an ill-posed problem, since more than one solution exists that reproduces the observations, and therefore constraints from a physical model or from other related disciplines (e.g. seismology, geology, seismics) disciplines are necessary. The density model gives an added piece of information to the existing seismic velocity model, as systematic differences in the relation between velocity and density give clues on the petrophysical rock composition as e.g. Bai et al. (2013) and Christensen and Mooney (1995). Moreover, the rheological rock parameters can be defined if both the seismic velocity and density are known. A particular focus of this work is on the lithospheric signatures of the magmatic

activity that affected the Alps from Paleozoic to Paleocene, which conditioned the mechanic characteristic of the crust during the Alpine phase, and in the phases preceding it (Castellarin et al., 2006; Viganò et al., 2013; Zampieri, 1995). The presence

35 of a gravity high located above the Venetian magmatic area comprising the Lessini Mountains, Berici and Euganei hills, and Rovigo has been known for decades (Braitenberg et al., 2013; Ebbing et al., 2006; Zanolla et al., 2006), but an explanation of the high is lacking. The present model shall define the mass sources through a 3D density modeling that starts from the recently acquired seismic tomography with improved spatial resolution (Kästle et al., 2018), thank's to the Alparray initiative (AlpArray Seismic Network, 2015).

40 Our 3D density modeling comprises the entire Alpine arc, and extends down to a depth of 200 km, the same depth of the seismic tomography model. The conversion from seismic velocity to density is done with differentiated approaches, depending on depth and position in upper crust, lower crust or mantle. We use the most recent terrestrial-satellite derived gravity model, and apply the global correction for terrain, which leads to very different Bouguer gravity values compared to the classic local correction up to the 167 km Hayford radius. The global fields require special attention and we include a dedicated study in

45 order to be used in the regional density modeling. The Alpine gravity field has been modelled before (Ebbing et al., 2006; Spooner et al., 2019), novel in our study is the use of the Bouguer field corrected for the global topography, which is more realistic than the 167 km classical Hayford radius reduction. A recent study (Spooner et al., 2019) used an approach in which density is constant for lateral crustal domains of typical extension of 80 km to 150 km, and the lithosphere is defined in layers of constant density. The layers have been defined with one layer for unconsolidated and consolidated sediments each, two

50 layers for crystalline crust, one layer for subcrustal lithosphere, and one constant layer for the asthenosphere. In our approach we do not pose any restrictions on the density variability, since we take full advantage of the high resolution seismic tomography model, and emphasis is put in our study to convert the seismic velocities to densities.

One of our central questions is whether we can demonstrate an alteration of the density structure or distribution in the crust and upper mantle below the extended Venetian magmatic Alpine province and the older Athesian magmatism (Bellieni et al.,

55 2010). Infact, during magmatic emplacement it can be expected that part of the molten crust is trapped in the lower crust. Only a portion (less than 10 wt%) of the entire molten rocks has erupted to the surface and less than 60 wt% of the whole melt can be emplaced as intrusions in the upper crust (De Min, personal comunication). Moreover, this crustal melting is often related to the emplacement of basic mantle derived magma at the Moho discontinuity (magmatic underplating), which provides the necessary temperature to induce a crustal melting.

60 The working hypothesis thus is, whether the above mentioned gravity high could be related to the different magmatic events that have affected the study area at different times, and the consequent crustal densification and/or juvenile crust formation in underplating.

2 Geological introduction

The study area comprises the Alpine arc, with particular focus on the magmatism of the southern Alps (Fig. 1). The southern Alpine domain represents the undeformed retro-wedge of an orogeny of double vergence (Dal Piaz et al., 2003; Zanchetta et al., 2012). To the north it is delimited by the dextral Periadriatic line, also known as Insubric line. The South-Alpine terrains
70 formed the passive margin of the Gondwana Paleozoic shelf (Muttoni et al., 2009; Stampfli and Borel, 2002). The central South-Alpine realms are characterized by three principal tectonic systems: the Val Sugana line, the Gudicarie line, and the Schio-Vicenza line, all active in the late Permian. The late Paleozoic-Meosozic rifting created a system of NS oriented faults, which induced the separation of the Lombardic basin from the Veneto platform, documented by the variable thickness of the Triassic and Cretaceous sediments (Bertotti et al., 1993). From the late Cretaceous to the first Eocene, the extensional regime
75 is inverted due to the convergence between Gondwana and Laurasia, which generates compressional systems which initiate to the west of the Gudicarie, and later extends to the eastern Dolomites (Zanchetta et al., 2012). Later, the Gudicarie is affected by two compressive phases; in mid-late Miocene the ENE-WSW oriented thrusts of the Valsugana develop, which exhume part of the Hercynian basement. In late Miocene and Pliocene the NE-SW oriented thrusts of Bassano and Grappa-Montello developed, together with reactivation of faults in the Gudicarie (Castellarin et al., 2006; Castellarin and Cantelli, 2000). From
80 end Paleozoic up to Tertiary different magmatic events have affected the South Alpine realm with intrusive and effusive products, that range from basic to acid. According to Castellarin and Cantelli, (2000) the volcanic and magmatic volumes have contributed to considerably increase the rigidity of the crust, with implications on the tectonics and geodynamics.

2.1 Permian Magmatism

The South Alpine units have been affected by large volumes of magmatism in the Paleozoic (285–260 Ma), with volcanic and
85 plutonic products, of acid and basic type (Rottura et al., 1998). The thickness of the deposits has an average value of 900 m, and reaches up to 2000 m (Rottura et al., 1998), and are represented by the ignimbrites and rare flows of the Athesian Volcanic District. These volcanic rocks are bordered by several outcropping granitic intrusion and the whole frame has some similarities with the coeval Ivrea-Verbano system (De Min, personal comunication), which has been interpreted as the remnants of a super-volcano (Quick et al., 2009). The units that belong to this age are the porpyhric Athesian platform, intrusions of Cima D'Asta,
90 Bressanone-Chiusa, Ivigna, Monte Croce, Monte Sabion, Monte Luco. These magmatic products indicate important crustal contamination which could be triggered by previous subduction (Variscan?), as indicated by their geochemichal properties (Rottura et al., 1998). The magmatism, probably has originated in a post-Hercynic phase in a trans-tensive tectonic regime. According to Rottura et al.(1998) the magmatism was generated due to a lithospheric thinning followed by:

- an asthenospheric upwelling,
95 - consequent partial melting of the asthenospheric mantle for adiabatic decompression,
- production of gabbro which, stored in underplating, has thermally perturbed the fertile crust,
- consequent production of crustal melts which mixed with most evolved mantle derived magma.

2.2 Triassic Magmatism

The Triassic magmatism affected a continental area which at the time confined with the western Tethys, and comprised the Southalpine, Dinaric, Transdanubian and Austral-alpine domains (Abbas et al., 2018). In the Dolomites the magmatic rocks are rare pyroclastics, dykes, sills, subaerial and marine volcanics, next to intrusives found at Predazzo and at Monti Monzoni. The origin of the magmatism has been hypothesized as due to a plume, subduction, or extensional events at lithospheric scale (Abbas et al., 2018; Casetta et al., 2018). The magmatism could be associated to activation of regional strike-slip faults during the Ladinian (Abbas et al., 2018). In comparison with the Paleozoic magmatic event, the Triassic magmatic volume appears to be more modest and characterized by a stronger abundance of basic and intermediate products. In the Dolomitic area these intrusions and vulcanites outcrop exactly inside the Permian magmatic structure. According to De Min et al. (2020) this could be related to the presence, in that time, of a restitic crust (depleted during the Paleozoic event) which scarcely interacted with the mantle derived melts stored in underplating. These latter could therefore have evolved without heavily contributing to a crustal fusion. Smaller outcrops of this event are also present along the Sugana valley and the Recoaro-Pasubio area.

2.3 Tertiary magmatism

From late Paleocene to Oligocene, during 25 Myrs, the terrains south of the Trento platform were affected by a volcanism that extended over an area of 2000 km2 (Milani et al., 1999). The principal units form the Lessini mountains, the Berici and the Euganei Hills. The province is characterized by basalts, basanites, transitional basalts and trachytes, which are divided in three categories according to the chemical composition, that ranges from alkaline to tholeiitic. The volcanic activity is due to an extensional regime that accompanied the formation of a foreland basin. The formation is connected to WNW-SSE compression originated from the Adria-Europe convergence during the Alpine orogeny (Macera et al., 2008; Milani et al., 1999; Zampieri, 1995). During this same period, the calc-alcaline intrusives of Adamello and Mesino-Bragaglia to the west of the southern Judicarie were emplaced. These batholiths are composed of several intrusive units that formed in Eocenic, in an interval between 31 and 35 Ma. Some Rb/Sr datings arrive up to 42 Ma for the location Corno Alto (Martin and Macera, 2014).

3 Geophysical Data

3.1 Seismic tomography database

The seismic tomography database from Kästle et al. (2018) is the starting point for the 3D density modeling. This recent model uses seismic stations distributed over the entire Alpine Arc, some stations in part of central Europe and many stations in Italy. The tomography of Kästle et al. (2018) analyses surface waves generated by earthquakes with periods between 8 s up to 250 s and ambient noise observations in a period range of 4 s to 60 s. Given the sensitivity of the seismic periods, the surface waves resolve the deep structures, the ambient noise records the crustal structure and sedimentary basins, with an overlap of the two records for periods between 10 s and 35 s. The tomography inversion uses the Ekström (2011) model as a starting model for

the inversion. The checkerboard test shows that the Alps and Italy are well resolved, except for the French territory, the Adriatic and Tyrrhenian seas. The Dinarides and Pannonian basin belong to the areas with less resolution. Some problems exist also in the resolution of superficial structures in the eastern Po-basin, due to scarce availability of seismic stations. The model resolves

135 the upper mantle well in the Alpine foreland of the Adria plate, of central Europe, of the Pannonian basin and the Ligurian Sea, with reduced resolution below the Alpine region. The model reports shear (Vs) velocities with a resolution in latitude of 0.1°, in longitude of 0.146°, and a vertical resolution of 100 m for the upper 600 m, of 500 m between 1 km and 2.5 km, of 1 km between 3 km and 12 km, of 2 km between 14 km and 84 km, and 5 km between 85 km and 200 km. The present study selects a portion of the model limited to longitudes 8 – 14 ° and latitudes 43 – 49 °.

140 **3.2 Gravity field and topographic reduction**

The gravity data are calculated from the global gravity model EIGEN6c4 (European Improved Gravity model of the Earth by new techniques (Förste et al., 2014a)). The model combines observations from different geodetic satellites, as LAGEOS-1/2 SLR, GRACE GPS-SST, GOCE and incorporates existing models from terrestrial data for the high frequency part. It uses the DTU 2'x2' global gravity anomaly grid from satellite altimetry (Andersen, 2010; Andersen et al., 2010) over the oceans and

145 the EGM2008 model (Pavlis et al., 2012) over the continents. The model consists in a table of spherical harmonic coefficients complete up to degree and order 2190. For degrees above N=235 in continental areas, the model reproduces the field of EGM08, over oceanic areas the model DTU12. The choice of the upper degree is justified by the fact that the authors of the model consider this maximum degree as adequate, and statistical evaluations have been made by the authors up to this degree (Förste et al., 2014b).

150 It is customary to reduce the gravity field for the effect of the topography, for which models in spherical harmonic expansion are available, as the model of Hirt et al. (2015) and Hirt and Rexer (2015). The layers building topography have been divided into glaciers, oceans, lakes and solid crust, with their respective homogeneous densities equal to 917 kg m^{-3}, 1000 kg m^{-3}, 1030 kg m^{-3}, 2670 kg m^{-3}. We have used the particular model dv_ELL_RET2014PLUSGRS80, which includes the gravity of the ellipsoid. We refer to Rexer et al. (2016) for details on how the model is obtained.

155 Due to the fact that several options exist in how to define the functional to obtain the gravity value from the spherical harmonic models of the earth gravity and the topographic effect, we briefly give here the fundamental definitions. Further details can be found for instance in the textbooks Torge (2011), Torge and Müller (2012) and Barthelmes (2013).

The Bouguer anomaly is defined as:

$$g_{bg} = g_{fa} - g^T \quad (1)$$

160 Here the gravity effect of the topography (g^T) is subtracted from the free-air anomaly (g_{fa}). The Free air anomaly according to Molodensky (Torge, 2011) is defined as:

$$\Delta g_{fa} = g(P) - \gamma(Q) \quad (2)$$

Eliminato: ,

Eliminato: New

Eliminato: ,

Formattato: Inglese (Stati Uniti)

Eliminato: .

with $g(P)$ the observed value in point P, and $\gamma(Q)$ is the gravity value of the reference ellipsoid calculated at the height of the telluroid. The gravity disturbance is defined as:

$$\delta g_{fa} = g(P) - \gamma(P) \qquad (3)$$

170 Here the gravity field of the ellipsoid is subtracted from the observed gravity field, both calculated in the observation point P. The gravity anomaly and gravity disturbance are related to the disturbing potential T (T(P) = W(P) - U(Q)) as follows:

$$\delta g_{fa} \approx -\frac{\partial(W-U)}{\partial h} \quad (4) \qquad \Delta g_{fa} \approx \delta g_{fa} - 2h^{-1}(W-U) \quad (5)$$

Here W is the earth gravity potential and U is the potential of the ellipsoid, and h is the geometric height. Vaníček et al. (2004) show that due to the second term which enters the definition of the gravity anomaly, the gravity disturbance must be used when
175 deriving the gravity potential of the topography for the Bouguer correction. Infact, otherwise the second term of Eq. (5) would be applied twice. In spectral domain the derivatives translate to the following:

$$\Delta g_{fa}(r,\lambda,\varphi) = \frac{GM}{r^2} + \sum_{n=0}^{N}\left(\frac{R}{r}\right)^n (n-1) \sum_{n=0}^{N}(C^T{}_{nm} \cos m\lambda + S^T{}_{nm} \sin m\lambda) P_{mn}(\sin\varphi) \quad (6)$$

$$\delta g_{fa}(r,\lambda,\varphi) = \frac{GM}{r^2} + \sum_{n=0}^{N}\left(\frac{R}{r}\right)^n (n+1) \sum_{n=0}^{N}(C^T{}_{nm} \cos m\lambda + S^T{}_{nm} \sin m\lambda) P_{mn}(\sin\varphi) \quad (7)$$

where $C^T{}_{nm}$ and $S^T{}_{nm}$ are the Stokes coefficients of the gravity potential of either earth or topography, to which the Stokes
180 coefficients of the ellipsoid have been subtracted. The calculated gravity anomaly and disturbance are shown in Fig. 2, and it is seen that the gravity disturbance is systematically higher than the gravity anomaly, confirming Vaníček et al. (2004). Subtracting the gravity effect of topography g^T calculated with the model RET2014 (Rexer et al., 2016) from the gravity disturbance derived from EIGEN6c4, the "Bouguer gravity disturbance" is obtained (Tenzer et al., 2019) (Fig. 3). This Bouguer field corresponds to the classical complete Bouguer anomaly, that includes both the topographic correction on top of the
185 Bouguer plate correction, with the difference that we consider the entire Earth, and do not limit the topographic corrections to the Hayford radius of 167 km. We fulfill all calculations (Barthelmes, 2013) with the publicly available gravity calculation service of ICGEM (International Center for Global Gravity Field Models; www.icgem.com). The result is a Bouguer map which is quite different from the one obtained from a local correction of the topography up to the Hayford radius of 167 km. Infact, the Bouguer values are -60 mGal over the Alpine arc, whereas the regional Bouguer values are classically below -180
190 mGal (e.g. Braitenberg et al., 2013; Ebbing et al., 2006; Spooner et al., 2019; Zanolla et al., 2006). Another area with clear negative values is close to the front of the Tuscan-Emilian Appennines, presumably due to the combined effect of sediments of the Po plain and the crustal thickening due to stacking of sediment layers of the Appennines. The markedly different values obtained with the global reduction are inherent to the distant masses that are neglected in the regional reduction, but which are largely compensated by the isostatic crustal thickness variations (Szwillus et al., 2016). The 3D density modeling we intend to
195 fulfil will be made on a window of less than 6° degrees latitude by 6° degrees in longitude, and a maximum depth of 200 km. The limit in lateral and depth extension of the model produces a bandlimited gravity field that can be modelled. It is therefore necessary to reduce the lowest degrees of the gravity field of topography, since they introduce a field which is due to distant

Eliminato:

Eliminato: e.g.

Eliminato: fulfill

masses and are uncorrelated to the regional properties of the gravity field which is going to be modelled in the present study. We find that starting with degree and order N>10 the field of topography starts resembling the regional topography, and use this value as lower limit for the spherical harmonic expansion of the fields. This value agrees with the findings of (Steinberger et al., 2010), who define degree 10 the limit of lithospheric contributions, lower degrees having their origin in the deep mantle

205 or lower. The band-limited Bouguer map obtained for degrees $10 < N \leq 2190$ (EIGEN 6c4 and RET2014) has the same features as the non-band-limited map, with the difference that now the Bouguer anomalies are more similar to those of the regional topographic reduction. Infact now the Bouguer disturbance is -160 mGal below the Alps, and -130 mGal below the Appennines.

4 Method

210 The aim of this work is to develop a three-dimensional density model of the Alpine region constrained by seismic tomography. The method is developed in four steps:

- Moho discontinuity investigation;

- Seismic wave velocity-density conversion for mantle and crustal layers;

- Gravimetric forward modelling and comparison between modelled results and the observed gravity data;

215 - Inversion of the gravimetric residual and model density correction

4.1 Moho discontinuity depth definition

The Moho discontinuity depth was defined by studying the vertical variation of the tomographic seismic velocity from Kästle et al. (2018). First of all, a preliminary velocity field analysis was fulfilled using other Moho models proposed by a) Tesauro et al.(2008) (EuCrust07), b) Laske et al.(2013) (Crust1.0), and c) Grad et al.(2009) (MohoGrad). From this field analysis it

220 was discovered that the mean S-wave velocity of the crust-mantle transition is 4.1 km s-1 with a standard deviation of 0.2 km s-1 (Table 1). This velocity value is in agreement with the velocity change at Moho between 3.85 km s-1 and 4.48 km s-1 proposed in the 1D global model AK135 (Kennett et al., 1995). Therefore, on the basis of this statistics, a preliminary result was obtained researching the maximum vertical gradient of the velocity profile, within a velocity range between 3.8 km s-1 and 4.4 km s-1, that represents the mean value plus and minus one standard deviation. To improve the stability and the

225 reliability of this approach, another condition has been imposed on the velocity surrounding the Moho surface obtained from the maximum gradient analysis. The S-wave velocity reported 4 km above and below the Moho surface must be respectively smaller and larger than the typical velocity of the lower crust and uppermost mantle. The mean P-wave velocity of the European lower crust is estimated to about 6.5 km s-1, while in the upper mantle, the P-wave velocity of the peridotite is larger than 8 km s-1 (Christensen and Mooney, 1995). From this observation, the limits for the P-wave velocity above and below the Moho

230 have been assigned to be of 6.8 km s-1 and 7.4 km s-1.

Eliminato: ,

Eliminato: (Tesauro et al., 2008) (EuCrust07) and (Laske et al., 2013) (Crust1.0).

The results show a good agreement with the Moho models proposed by the other authors (Fig. 4). Some differences are represented by an important crustal thickening located in the Ivrea-Verbano (D1) area and below the Istrian region (D2). Also the geometry and the depth found for the two main orogens (D3) are significantly different from the reference models, and our model seems to have a better resolution.

4.2 Seismic wave velocity to density conversion for mantle and crustal layers

The Moho discontinuity allowed to divide the entire tomographic volume in crustal and mantle layer. For each layer, a different approach and relations were used, in order to define the density values starting from the tomographic seismic velocity.

4.2.1 Crustal conversion

A huge set of relations were proposed by different authors in order to convert the seismic wave velocity in density (Brocher, 2005) and most of these equations were found to transform principally the compressional wave velocity (Vp) to density. For this reason, it has been necessary to convert the tomographic Vs in Vp through the "Brocher's regression fit" (Brocher, 2005), a relation obtained from seismic, borehole and laboratory data for different kinds of lithology and valid for Vs between 0 and 4.5 km s^{-1}. Given the extreme variability of the crustal rocks present in the study area, a density estimation was carried out through two equations: the "Gardner's rule" by Gardner et al.(1974) and the "Linear regression fit" proposed by (Christensen and Mooney (1995). The first is an empirically derived equation that relates seismic P-wave velocity to the bulk density of the lithology. It is very popular in petroleum exploration because it can provide information about the sedimentary lithology from interval velocities obtained from seismic data. On the other hand, Christensen and Mooney (1995) proposed a widely used linear density-Vp relation for crystalline rocks obtained from seismic refraction and laboratory data, in order to define the continental crust features as a function of the different geodynamic context. In this work, for distinguishing the sedimentary rocks velocity domain from the crystalline domain, and therefore which of the two relations to use, the velocity value of Vp = 6 km s^{-1}, at which the two curves intersect as seen in Fig. 5 and also in Brocher (2005), has been chosen.

4.2.2 Mantle conversion

A different approach has been used for the velocity conversion in the upper-most mantle; in this case, the tomographic velocity model was compared with a Synthetic Upper Mantle model (SUM). The SUM was modelled through the open-source software Perple_X (Connolly, 2005), which allows the computation and mapping of the phase equilibria, rheological properties and density.

For this modelling the TECTON bulk rock composition model (Griffin et al., 2009) of the mantle has been used, which represents an estimate of the mean composition of a Neoproterozoic-Phanerozoic Sub-Continental Lithospheric Mantle (SCLM), gained from xenolith suites and peridotite massifs data. In Table A-1, the major elements of the TECTON composition are shown, of which we used the most abundant elements, up to a total content of 98.9 %, leaving out the minor elements with percentages less than 1 %. The software calculates the stable phases for a two-dimensional grid of temperature

Eliminato:

Eliminato:

Eliminato:

Eliminato:

Eliminato:

Eliminato:

Eliminato:

Formattato: Non Evidenziato

Eliminato:

Eliminato: intersect

Eliminato: (Fig. 5). The velocity is Vp = 6 km s^{-1}, as seen in (Brocher, 2005) and Fig. 5

(T) and pressure (P) conditions, typical for the mantle up to a depth of 200 km (Tmin=350 °C to Tmax=1600 °C, Pmin=0.1 GPa to Pmax=7 GPa). The software requires setting some calculation parameters, which are defined here. The thermodynamic model is the Holland and Powell (1998) model, which is the default. For the computation of the phase equilibria and the elastic properties, the default parameters have been used. Further options included: no presence of saturated fluids, calculation with

280   saturated components not present, chemical potentials, activities and fugacities are not independent variables. The adopted mineral phases for the synthetic mantle SUM are: Olivine, Clinopyroxenes, Orthopyroxenes, Garnet, Spinel and Plagioclase and the thermodynamic model for these solid solutions is again the Holland and Powell (1998) database. We refer to the documentation of the software and the original paper for the thermodynamic modeling details, which are out of scope of the present work.

285   The result consists in the equilibrium phase diagram, which shows the fields of stability of different equilibrium mineral assemblages for the adopted bulk-rock composition, depending on the P-T combinations. For each assemblage a number of parameters are given as well, from which we select Vs and density, shown in Fig. 6.

The conversion of the seismic velocity to density was made comparing the tomographic velocity at its given depth, with the synthetic velocity at the pressure corresponding to the depth. The pressure was calculated integrating the lithospheric density

290   column from top to the corresponding depth. From the topography to the bottom of the crust, the crustal density model calculated from the crustal seismic velocities was used. The resulting pressure at the base of the crust was used for converting the seismic velocity to density in the resolution cell below the Moho, and then iteratively downwards to the base of the model. The temperature was left unconstrained and corresponds to the value that allows to match the tomographic and synthetic velocity at the given pressure. The above described density values define the starting model which is corrected through the

295   gravity inversion discussed in the next chapters.

4.3 Gravimetric forward modelling and comparison between modelled results and the observed gravity data

In the previous section it has been argued how the P-wave velocities were transformed into density values. The next step was to discretize the entire model with tesseroids, mass elements defined in spherical geocentric coordinates (Anderson, 1976; Grombein et al., 2013; Heck and Seitz, 2007; Wild-Pfeiffer, 2008). This task has been done building these elements as function

300   of the original three-dimensional tomographic grid, from which we defined the density value of the tesseroids. In order to make the modelled gravity effect comparable with the observed gravity anomaly, the obtained density model was reduced by the reference density model PREM ("Preliminary Reference Earth model"). This one-dimensional reference model represents the mean physical features of the earth, including elastic parameters, seismic attenuation, density, pressure and the earth-radius dependent gravitational value. Being a global model, it was modified in order to obtain a one-dimensional model comparable

305   with a continental crust, eliminating the first 3 km of seawater and lowering the Moho depth. All changes to the original PREM model have been done to maintain the pressure value at the base of the model constant and we call this modified model co-PREM (Fig. A1 in Appendix).

The Fig. 7 (a) shows the result of the gravitational forward modelling, developed through the software Tesseroids (Uieda et al., 2016). The gravity anomaly map presents two well defined negative anomalies induced by the crustal thickening below the orogens and the extensive positive anomaly produced by the Tyrrhenian crust. At large scale, the modelled anomaly reproduces in broad outline the observed data (Fig. 3c) and from the difference between observed-modelled anomalies, we obtained the residual gravity map (Fig. 7). The residual map shows that the modelled anomaly differs from the observed map by values that range from –40 mGal to +220 mGal. Furthermore, the residual outlines three regions characterized by different trends: Germany and part of Switzerland are characterized by negative values reaching peaks around –40 mGal (A1), the Tyrrhenian basin shows a positive residual around +80 mGal (A2), while the residuals are generally positive in all of the remainder study area, reaching values of +200 mGal (A3).

4.4 Inversion of the gravimetric residual and model density correction

Theoretically, the gravity residual map represents the extent to which the starting density model diverges from the one of the infinite possible density distributions that produced the measured gravity anomaly. In order to improve the reliability of the starting density model an inversion algorithm was developed based on the residual between observed and modelled data. As seen in the Fig. 8, the first step is to separate the long wavelength residual component from the short wavelengths, and to estimate the different contributions of the mass sources that generate the residual signal.

The distinction between crustal and mantle contribution, which corresponds to the long and short wavelengths respectively, has been done by fitting a third-order polynomial surface with the values of the residual map (Fig. 9), and the choice of the order was made by a qualitative evaluation depending on the features and the large scale trend of the residual anomaly map.

The evaluation consisted in the observation that increasing the degree starting from zero added long wavelength signal to the mantle component, which is uncorrelated to both topography and geology. Starting with degrees higher than 3 the polynomial started to show smaller scale features which correlated with the geometrical and physical properties of the crust. We therefore think that the third order polynome is qualitatively the correct choice to separate the mantle from the crustal component. The mantle component has a long period trend oriented NW–SE. The third order polynome allows to separate this very long-wavelength signal from the crustal contribution.

Then, once we have obtained the two components, the algorithm provided the "linear iterative inversion" section, in which a rough first density correction was computed with the "Infinite slabs gravimetric effect" equation:

$$\Delta \rho = \frac{\Delta g}{2\pi G H} \quad (8)$$

where $\Delta \rho$ is the density correction, Δg is the short or long gravimetric residual component, H represents the thickness of the considered layer (crustal or mantle layer) and G is the gravitational constant. Then the density correction was applied to the starting density model, the vertical distribution of the total mass correction has been assigned through the following equation:

$$\rho_{i\_new}(z) = \rho_{i\_old}(z) + \Delta \rho_n H_n \left(\frac{\rho_{i\_old}(z)}{\sum_{i=1}^{N} \rho_{i\_old}(z) \Delta z_i} \right) \quad (9)$$

Commentato [CB1]: Davide: Indicare in Fig. 7

Eliminato: the Tyrrhenian basin shows a positive residual around +80 mGal,

Eliminato: is

Eliminato: ,

Eliminato: provides

Eliminato: is

Eliminato: is

where ρ_{i_new} and ρ_{i_old} are respectively the new and the old density values, $\Delta\rho_n$ is the density correction, H_n is the height of the considered layer (crust or mantle layer) and Δz_i represent the height of the mass element belong the single density profile. We applied the density correction, obtained a new mass distribution, and computed the forward modelling of the corrected density model in the next step. The results of the latter operation was compared with the observed data producing, for each iteration, a new gravimetric residual map. The iteration was stopped when the root mean square residual reached the value of 3 mGal.This algorithm allowed to define a density correction, which was applied to the three-dimensional starting model and allowed to compare the gravity effect of this new mass distribution with the observed data.

5 Results

5.1 Alpine region density distribution

Figure 10 shows horizontal slices of the final density model at increasing depths ranging between 5 km and 40 km. Here we describe the main features.

In the first kilometres, up to 15 km depth (Fig. 10 (a),(b),(c)), the low density values are due to the two main sedimentary basins situated in the fore-deeps of Alps and Apennines. In the European plate, the Molasse basin develops in W–E direction along the northern Alps front (LMB), and this sedimentary layer is wider and thinner in the western part whilst it straitens and thickens in the eastern Bavarian part. In the Adriatic plate, the Po basin (PBL) is characterized by a thicker and less dense sedimentary layer than the Molasse basin. The Molasse basin is shallower (average thickness 5 km, maximum thickness 9 km), than the Po basin (average thickness 9 km, maximum thickness 13 km). As shown in Fig. 10 (a) and 10 (b), both modelled basins show a progressive decrease of the densities towards the eastern part of the sedimentary layer (especially at the south of the Po river mouth).

Always in the first 15 kilometres, a homogenous density region (2650–2750 kg m^{-3}) features the Alpine orogenic upper crust. Inside this domain a relative low-density anomaly (2650 kg m^{-3}), corresponding to the Helvetic nappe (HL) and the Tauern window (TWL) is present, while in the Ivrea-Verbano (IVH) zone the density reaches the typical values of the lower crust (2850–2900 kg m^{-3}).

Between 15 and 20km (Fig. 10(c) and 10(d)) the modelled density represents the gradual transition from upper to lower crust, except in the Tyrrhenian basin (TBH), where the high density values indicate the crust-mantle transition, in agreement with the Moho depths of Fig 4d. In this depth-interval, the Adriatic crust is denser than the European crust; furthermore, a W–E trending high-density value ridge (RH) (2900 kg m^{-3}) follows the western South-Alpine domains, passing near the Schio-Vicenza fault up to the buried front of the Apennines. As previously seen in the first kilometres, a relative low density domain remains below the Helvetic terrain (HL) and the Tauern window (TWL); a further lower density patch is present in the Adriatic sea, below the northern Apennines (PBL), and facing the Valsugana thrust system (BBL).

Figures 10(e) and 10(f) show the lower crustal modelled density of the European and Adriatic plates, where the relatively low-density values characterising the lower crust of the inner part of the Alpine and Appennine orogens (2800–2850 kg m^{-3}) are

Eliminato: apply

Eliminato: is

Eliminato: allows

Eliminato: is

Eliminato: allows

visible (IPL), while in the outer parts of the two orogens and in the foredeep regions (OPH), the average density is higher
385 (2900–2950 kg m^{-3}). Very high values affect the lower crust of the north-western part of the study area, close to the Upper
Rhine graben system (GSH) and, furthermore, the W–E trending high-density ridge is still present (RH), reaching higher values
at this depth (up to 3000 kg m^{-3} below the Giudicarie and Schio-Vicenza fault system). At 30 km depth, mantle density is
present in the Northern European plate and Adriatic Sea, in agreement with the Moho depths of Fig 4d.
At greater depth (Fig. 10(g) and 10(h)), the modelled density features of the Alps and Apennines crustal roots and the inner
390 part (LIP) of the two belts are characterized by lower densities (2800–2850 kg m^{-3}) than the surroundings. Beyond the orogens
crustal roots, the mantle is marked by a density average around 3300 kg m^{-3}.
We have computed also the weighted average density for the crustal layer (Fig. 11). The average density distribution
reproduces and synthesizes all the features seen above. In the European plate, different domains are present for the area close
to the Upper Rhine Graben (GSH) (high-density 2860–2900 kg m^{-3}) and the Molasse basin (MBL) (2740–2800 kg m^{-3}). Also,
395 the Alps show a density zonation in good agreement with the surface geology: Helvetic terrain (HL) and Tauern window
(TWL) are on average less dense than the Penninic (PH), Austroalpine (AH) and Southalpine (SH) nappes. The Adriatic
domain is represented by a highly complex density distribution with a heterogeneous low-density area highlighting the Po
basin (PBL), the adjacent Adriatic and other two more restricted areas situated in the Piedmont (PDL) and Venetian basins
(BBL) regions. In the Apennines, the density values follow the main structural lines defined by the stack of NE to E verging
400 thrust fronts and the back-arc basin affected by extensional tectonics. In the South Alpine domain, the model generally shows
high-density values, especially in the Ivrea-Verbano complex (IVH) (3000 kg m^{-3}) and at the Valsugana thrust system (SH)
(2870 kg m^{-3}) in the eastern part. The previously discussed W–E high-density ridge which develops from the Ivrea-Verbano
anomaly to Schio-Vicenza fault system (RH), and that affects the Trento platform, is also seen in the average crustal density
map.
405

5.2 Modelled density in the Venetian gravity anomaly area

Three representative transects across the main gravity anomaly structures of the central-eastern Southern Alps are illustrated
in Fig. 12, and discussed in the following.
The A section (Fig. 12) shows the density distribution along the main direction of the positive gravity anomaly, parallel to the
410 Schio-Vicenza fault. The low density in the southern part of the profile, represents the sediment layer that reaches a thickness
of around 13 km in the deepest part (longitude 12.5° E in the profile). As seen before, between the South-Giudicarie fault
(SGF) and the buried Appennines thrust front, there is again the high-density plateau (RH) situated between 25km and the
Moho discontinuity, with a density of 2900–3000 kg m^{-3}. In the middle crust, two limited mushroom-shaped bodies are lying
between 10 and 25 km, the first (MB1) is located below the Venetian Volcanic Province (VVP) and above the high-density

plateau (RH) close to latitude 11.5° N, while the second (MB2) is situated below an area between the south Giudicarie fault (SGF) and the Periadriatic Line (PL) corresponding to the outcropping Adamello batholith (AB).

The NE-SW oriented section (Fig. 12 – B section), is orthogonal to the well-developed sedimentary wedge of the Alpine and Apennines foredeep (PB), which is 10 km thick in the deepest part and has density values between 2350 up to 2550 kg m^{-3}.

425 Using the 2700 kg m^{-3} contour line as a marker of the top of the Mesozoic carbonate platform, it is possible to note that the contour line depth increases between latitude 46° N and latitude 44° N. The 2700 kg m^{-3} contour line reaches the surface in front of the Valsugana thrust system (at around 46° N latitude) (Fantoni and Franciosi, 2010). North of the Valsugana thrust front (VTF), corresponding to the southern alpine belt, the model shows density values of 2750 kg m^{-3} for the upper crust and 2800 up to 2900 kg m^{-3} for the middle-lower crust. In the central part of the section the model reports a very high-density

430 plateau (RH) situated in the lower crust, that develops from the Apenninic buried thrust front (ATF) up to the outcropping south-vergent thrust (VTF).

The last section (close to W–E) crosses the Ivrea-Verbano area (Fig. 12 – section C), and then runs along the Po sediment basin. Lateral density variations of the upper crust are well correlated with the different basin domains represented from west to east by the Lombardian basin (LB), the Trento platform (TP) and the Belluno basin (BB). The mid-crust shows high-density

435 (e.g. greater than 2800 kg m^{-3}) values already at a depth of 20 km, and this value distribution corresponds to the previously discussed high-density ridge (RH) seen in the average density map (Fig. 11).

6 Discussion

Several geophysical models have been developed for the Alpine lithosphere in the past, especially using seismic (Gebrande et al., 2006; Kästle et al., 2018) and gravity data as modelling constraints (Ebbing et al., 2006; Spooner et al., 2019). In this work

440 for the first time, a high resolution three-dimensional seismic tomography model has been adopted as starting model for the computation of a 3D density model using the algorithm discussed before. The results show a highly complex density distribution in good agreement with the different geological domains of the Alpine area represented by the European plate, the Adriatic plate and the Tyrrhenian basin. Notwithstanding the offsets that can occur between the outcropping geology, and the intracrustal tectonic domains, we find that the average crustal density map correlates with the different tectonic realms.

445 The Adriatic derived terrains (Southalpine and Austrolpine) of the Alps are typically denser (2850 kg m^{-3}), whilst the Alpine zone composed by European terrains provenance (Helvetic and Tauern window) presents lower density values (2750 kg m^{-3}). This density relation has been also noted by Spooner et al. (2019), indicating that this physical parameter could be used as a marker for the different tectonic domains.

The South-Alpine and Austroalpine provinces, were the locus of sporadic, yet occasionally widespread magmatism. The

450 magmatic occurrences are associated with strongly variable tectonic regimes, which range from clearly collision-related (the Austroalpine Paleogene plutonism, i.e., Vedrette di Ries/Riesen Ferner), to late- or slightly post-orogenic associated with basin formations shortly after the main Variscan orogeny (Permian magmatism, e.g., the Athesian Volcanism and Ivrea Verbano and

Eliminato:

Serie dei Laghi Group), to clearly post-orogenic (Triassic, e.g., the Predazzo–Monzoni complexes), and finally to an almost
455 within-plate environment, peripheral to the Alpine belt (the Oligocene Veneto Volcanic province) (Bellieni et al., 2010).
These magmatic activities have undoubtedly changed the thermal setting at the time and, after cooling, increased the crustal
rigidity especially in the Venetian Alps (Dolomites) which appears today the least deformed and shortened in the whole
Southern Alps domain (Castellarin et al., 2006).

In this domain, south of the Dolomites, the well-known positive Bouguer gravity anomaly is present, located between the
460 towns of Verona and Vicenza, which covers the Venetian Volcanic Province (VVP). The short-wavelength content of this
gravity high can reasonably be explained by the presence of a shallow Mesozoic carbonate platform (Trento Platform) and
basement which hosted several volcanic bodies, as demonstrated by field evidence and the intra-sedimentary magnetic bodies
proposed by Cassano et al. (1986) on the base of magnetic and well data. According to this interpretation, the isolated
mushroom-shaped body modelled in the middle-upper crust could be related to the Triassic and Cenozoic magmatic activity.
465 These intrusions develop below the Venetian Volcanic Province and could correspond to the Predazzo-Monzoni complex and
the Adamello and Mesino-Bragaglia plutons emplaced respectively in the Dolomites and westward of the South-Giudicarie
fault. However, the remainder part of this signal corresponds to signal generated by the lower crustal source component, which
gives origin to the long wavelength of the positive Bouguer anomaly, as also proposed by Zanolla et al. (2006). During
Permian, the Austroalpine and Southalpine units were affected by magmatism, high-temperature/low-pressure metamorphism
470 (HT-LP) and extensional tectonics. Intra-continental basins hosting Permian volcanic products have been interpreted as
developed either in a late-collisional strike-slip or in a continental rifting setting (Spalla et al., 2014; Spiess et al., 2010 and
references therein). As regards the geodynamic context, all evidence suggests that this magmatic pulse was induced by post-
Variscan lithospheric attenuation that produced crust-mantle detachment and large ultra-mafic crustal underplating, together
with the development of a Permian basin (Dal Piaz and Martin, 1998). For a fuller understanding of this process, we may refer
475 to the modern model tested in the Western Southern Alps, in the Ivrea-Verbano zone, where the entire crustal section of an
underplated and metamorphosed Hercynian basement crops out, overlain by volcanic and sediment formations (Quick et al.,
2009, 1995; Sinigoi et al., 2011). In the central Southern Alps the Permian activity is represented by the porphyry plateau of
the Bolzano province (Athesian plateau) and the numerous granitic–granodioritic intrusions. Considering the large scale of
this process, it is reasonable to suppose the scattered presence of mafic underplating in the whole Alpine realm, confirmed by
480 the Permian–Triassic gabbro bodies and related HT-LP metamorphism emplaced in the Austro-Alpine and South-Alpine
continental crust (Spalla et al., 2014). According to this hypothesis, the high-density values modelled for the Adriatic lower
crust (high-density ridge HR, Fig. 10 (d) – (f)) are consistent with the densities of a basaltic mantle-derived rock, hence this
anomalous lower crust could be interpreted as mafic underplating emplaced between the crustal-mantle transition during
Permo-Triassic post-collisional lithospheric extension.

485 Historically, the deep source of the Vicenza-Verona positive gravity anomaly has been explained by thinned crust of 25-27
km (Cassinis, 2006; Finetti, 2005; Gebrande et al., 2006; Scarascia and Cassinis, 1997). This approach has been promoting the
development of several Moho models of the Alps that invoke a relatively shallow mantle situated in the central-southern alps,

490 especially for the gravity-modelling derived Moho models (Braitenberg et al., 2002; Ebbing et al., 2001). Recently, other seismic methodologies such as local earthquake tomography, receiver functions and ambient noise tomography, have allowed to develop 3-D high-quality crustal models of the Alps (Kästle et al., 2018; Spada et al., 2013), and this family of Moho models point to a crustal thickness of 30-35 km in the Vicenza-Verona positive gravity anomaly region, corroborating the possibility that the gravimetric anomaly is related to an intra-crustal denser source (mafic underplating). Also Mueller and Talwani (1971)

495 in their Alpine crustal model, proposed high density distribution for the South Alpine lower crust, that connects the Venetian gravity high with the Ivrea-Verbano zone.

Unfortunately, the kinematics of magmatic underplating has been described mainly by petrophysical models explaining the genesis of the outcropping rocks, while the available geophysical images of underplated material remain relatively sparse and confined to specific tectonic environments (Thybo and Artemieva, 2013). Our work adds a geophysical model based on the

500 gravity field to demonstrate the existence of underplating to an area related to an orogen. Underplating from a gravimetrc analysis had been postulated for instance also in the context of the Parana' large igneous province (Mariani et al., 2013), the Chad basin (Maddaloni et al., 2020), and the West Siberian large igneous province (Braitenberg and Ebbing, 2009).

7 Conclusion

The scope of this work is to study the density distribution of the Alpine lithosphere, with the specific target of characterising

505 the sources of the well-known Venetian gravity anomaly high. A new approach based on three-dimensional seismic tomography as starting model for the computation of a 3D density model has been developed. We propose an innovative approach which includes several numerical algorithms and that provides a Moho definition, a velocity-density conversion, gravimetrical forward modelling and finally a linear inversion based on the gravimetric residual map. The results for the Alpine structure highlight that all terrains of Adriatic provenance (Austro-Alpine and South-Alpine) are denser (2850 kg m^{-3}) than the

510 European terrains (2750 kg m^{-3}), suggesting that this physical parameter could be used as a marker to characterize the different tectonic domains involved in the Alpine regions (Spooner et al., 2019).

The studied gravity anomaly is located in the central South-Alpine domain, this area being the locus of several magmatic and volcanic activities developed from Carboniferous up to the Paleogene (Athesian Volcanic, Predazzo – Monzoni and Venetian Volcanic Province) which has modified the rheological and thermal settings. The results of our density model suggests that

515 the gravity anomaly sources could be related to:

- Localized mushroom-shaped magmatic bodies intruded into the middle-upper crust, which could correspond to the Triassic and Cenozoic Predazzo-Monzoni, Mesino-Bregaglia and Adamello plutons, nowadays outcropping in the Southern Alps,
- Mafic underplating emplaced in the lower crust during the Permian lithosphere attenuation, similarly to the

520 model developed for the Ivrea-Verbano complex present in the western part of the Southern Alps.

We also considered the alternative source models for this gravity anomaly, in which different authors provide a stretched and
525 thinned Adriatic crust located between the Giudicarie thrust front and the Schio-Vicenza fault, but today several Moho models
of the Alps exist, that refute this model.

The approach we use, could represent a generally applicable method to achieve insights about large-scale crustal density
distributions, starting from seismic tomography, and it allowed us to carry out a high-resolution density model for the Alpine
region. The expected improvement of more robust and high-resolution seismic tomography models, as well as the development
530 of a non-linear inversion algorithm, could enhance the reliability of the density models in the future.

Appendices

535

	TECTON Avg. SCLM comp.
SiO_2	**44.50**
TiO_2	**0.14**
AlO_3	**3.50**
Cr_2O_3	**0.40**
FeO	**8.0**
MnO	**0.13**
MgO	**39.8**
CaO	**3.10**
Na_2O	**0.24**
NiO	**0.26**

550

**Table A1 Median composition of the sublithospheric continental mantle (SLCM) normalized to 100% used for the modeling of the
density to seismic velocity conversion, dependent on temperature and pressure conditions** (Griffin et al., 2009)
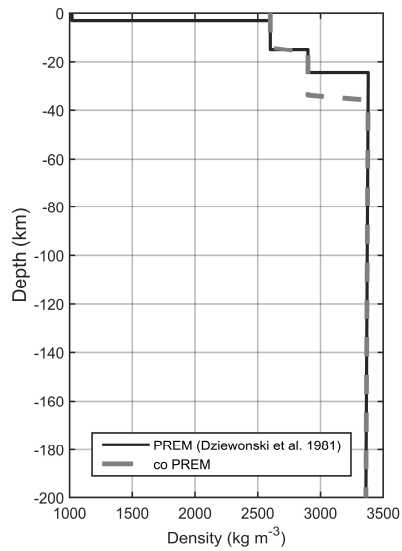
Figure A1 Density of the PREM model and the modified coPREM model used as reference in the modeling procedure.

555

Data Availability

The 3D density model is available in the publicly accessible repository zenodo.org at

560 link https://www.zenodo.org/record/3885404#.Xt5IHzozbIV.

Author Contributions

Both authors contributed to the conception and design of the study, manuscript writing, and approved the submitted version.
Davide Tadiello was in charge of all computations.

Funding

565 The work was partly supported by projects ASI N. 2019-16-U.0, CUP F44117000030005 and by project PRIN 2017
20177BX42Z

Conflict of Interest

The authors declare that the research was conducted in the absence of any commercial or financial relationships that could be construed as a potential conflict of interest.

Acknowledgements

We thank E. Kästle and L. Boschi for sharing their tomographic model and for helpful discussions. We also thank for helpful discussions on the petrologic modeling M. Velicogna, A. De Min, M. Tesauro and for assistance in using the Perple_X software L. Ziberna. T. Pivetta and A. Pastorutti are thanked for assistance in Matlab programming and helpful discussions.

References

Abbas, H., Michail, M., Cifelli, F., Mattei, M., Gianolla, P., Lustrino, M., Carminati, E., 2018. Emplacement modes of the Ladinian plutonic rocks of the Dolomites: Insights from anisotropy of magnetic susceptibility. Journal of Structural Geology 113, 42–61. https://doi.org/10.1016/j.jsg.2018.05.012

AlpArray Seismic Network, 2015. AlpArray Seismic Network (AASN) temporary component. https://doi.org/10.12686/ALPARRAY/Z3_2015

Andersen, O.B., 2010. The DTU10 Gravity field and Mean sea surface. Presented at the Second international symposium of the gravity field of the Earth (IGFS2), Fairbanks, Alaska., Second international symposium of the gravity field of the Earth (IGFS2), Fairbanks, Alaska.

Andersen, O.B., Knudsen, P., Berry, P.A.M., 2010. The DNSC08GRA global marine gravity field from double retracked satellite altimetry. J Geod 84, 191–199. https://doi.org/10.1007/s00190-009-0355-9

Anderson, E.G., 1976. Anderson EG (1976) The effect of topography on solutions of Stokes' problem. Unisurv S-14, Rep, School of Surveying, University of New South Wales, Australia.

Bai, Z., Zhang, S., Braitenberg, C., 2013. Crustal density structure from 3D gravity modeling beneath Himalaya and Lhasa blocks, Tibet. Journal of Asian Earth Sciences 78, 301–317. https://doi.org/10.1016/j.jseaes.2012.12.035

Barthelmes, F., 2013. Definition of Functionals of the Geopotential and Their Calculation from Spherical Harmonic Models. Scientific Technical Report (STR) STR 09/02, 1–32. https://doi.org/10.2312/GFZ.b103-0902-26

Bellieni, G., Fioretti, A.M., Marzoli, A., Visonà, D., 2010. Permo–Paleogene magmatism in the eastern Alps. Rend. Fis. Acc. Lincei 21, 51–71. https://doi.org/10.1007/s12210-010-0095-z

Bertotti, G., Picotti, V., Bernoulli, D., Castellarin, A., 1993. From rifting to drifting: tectonic evolution of the South-Alpine upper crust from the Triassic to the Early Cretaceous. Sedimentary Geology 86, 53–76. https://doi.org/10.1016/0037-0738(93)90133-P

Bigi, G., Castellarin, A., Coli, M., Dal Piaz, G.V., Sartori, R., Scandone, P., Vai, G.B., 1990a. Structural Model of Italy scale 1:500.000, sheet 1. Structural Model of Italy scale 1:500.000, sheet 1.

Bigi, G., Castellarin, A., Coli, M., Dal Piaz, G.V., Vai, G.B., 1990b. Structural Model of Italy scale 1:500.000, sheet 2. Structural Model of Italy scale 1:500.000, sheet 2.

Braitenberg, C., Ebbing, J., 2009. New insights into the basement structure of the West Siberian Basin from forward and inverse modeling of GRACE satellite gravity data. Journal of Geophysical Research: Solid Earth 114. https://doi.org/10.1029/2008JB005799

Braitenberg, C., Ebbing, J., Götze, H.-J., 2002. Inverse modelling of elastic thickness by convolution method - The eastern Alps as a case example. Earth and Planetary Science Letters 202, 387–404. https://doi.org/10.1016/S0012-821X(02)00793-8

Braitenberg, C., Mariani, P., De Min, A., 2013. The European Alps and Nearby Orogenic Belts Sensed by GOCE. Boll. Geofis. Teor. Appl. 54, 321–334. https://doi.org/10.4430/bgta0105

Brocher, T.M., 2005. Empirical Relations between Elastic Wavespeeds and Density in the Earth's Crust. Bulletin of the Seismological Society of America 95, 2081–2092. https://doi.org/10.1785/0120050077

Casetta, F., Coltorti, M., Marrocchino, E., 2018. Petrological evolution of the Middle Triassic Predazzo Intrusive Complex, Italian Alps. International Geology Review 60, 977–997. https://doi.org/10.1080/00206814.2017.1363676

Cassano, E., Anelli, L., Fichera, R., Cappelli, V., 1986. Pianura Padana: interpretazione integrata di dati geofisici e geologici. Presented at the 73° Congresso SocietàGeologica Italiana, Roma, 29 Settembre - 4 ottobre 1986, pp. 1–28.

Cassinis, R., 2006. Reviewing pre-TRANSALP DSS models. Tectonophysics, TRANSALP 414, 79–86. https://doi.org/10.1016/j.tecto.2005.10.026

Castellarin, A., Cantelli, L., 2000. Neo-Alpine evolution of the Southern Eastern Alps. Journal of Geodynamics 30, 251–274. https://doi.org/10.1016/S0264-3707(99)00036-8

Castellarin, A., Vai, G.B., Cantelli, L., 2006. The Alpine evolution of the Southern Alps around the Giudicarie faults: A Late Cretaceous to Early Eocene transfer zone. Tectonophysics 414, 203–223. https://doi.org/10.1016/j.tecto.2005.10.019

Christensen, N.I., Mooney, W.D., 1995. Seismic velocity structure and composition of the continental crust: A global view. Journal of Geophysical Research: Solid Earth 100, 9761–9788. https://doi.org/10.1029/95JB00259

Connolly, J.A.D., 2005. Computation of phase equilibria by linear programming: A tool for geodynamic modeling and its application to subduction zone decarbonation. Earth and Planetary Science Letters 236, 524–541. https://doi.org/10.1016/j.epsl.2005.04.033

Dal Piaz, G.V., Bistacchi, A., Massironi, M., 2003. Geological outline of the Alps. Episodes 26, 175–180. https://doi.org/10.18814/epiiugs/2003/v26i3/004

Dal Piaz, G.V., Martin, S., 1998. Evoluzione litosferica e magmatismo nel dominio austro-sudalpino dall'orogenesi varisica al rifting mesozoico. Memorie della Società Geologica Italiana 53, 43–62.

De Min, A., Velicogna, M., Ziberna, L., Chiaradia, M., Alberti, A., Marzoli, A., 2020. Triassic magmatism in the European Southern Alps as an early phase of Pangea break-up. Geol. Mag. 1–23. https://doi.org/10.1017/S0016756820000084

Ebbing, J., Braitenberg, C., Götze, H.-J., 2006. The lithospheric density structure of the Eastern Alps. Tectonophysics 414, 145–155. https://doi.org/10.1016/j.tecto.2005.10.015

Ebbing, J., Braitenberg, C., Götze, H.-J., 2001. Forward and inverse modelling of gravity revealing insight into crustal structures of the Eastern Alps. Tectonophysics 337, 191–208. https://doi.org/10.1016/S0040-1951(01)00119-6

Ekström, G., 2011. A global model of Love and Rayleigh surface wave dispersion and anisotropy, 25-250 s: Global dispersion model GDM52. Geophysical Journal International 187, 1668–1686. https://doi.org/10.1111/j.1365-246X.2011.05225.x

Fantoni, R., Franciosi, R., 2010. Tectono-sedimentary setting of the Po Plain and Adriatic foreland. Rend. Fis. Acc. Lincei 21, 197–209. https://doi.org/10.1007/s12210-010-0102-4

Finetti, I.R., 2005. Depth Contour Map of the Moho Discontinuity in the Central Mediterranean Region from New CROP Seismic Data. Presented at the Finetti, I.R. (Ed.) CROP Project: Deep Seismic Exploration of the Central Mediterranean and Italy, Elsevier, Atlases in Geoscience, Amsterdam, Netherlands, pp. 597–606.

Förste, C., Bruinsma, S., Abrikosov, O., Flechtner, F., Marty, J.-C., Lemoine, J.-M., Dahle, C., Neumayer, H., Barthelmes, F., König, R., others, 2014a. EIGEN-6C4-The latest combined global gravity field model including GOCE data up to degree and order 1949 of GFZ Potsdam and GRGS Toulouse, in: EGU General Assembly Conference Abstracts.

Förste, C., Bruinsma, Sean.L., Abrikosov, O., Lemoine, J.-M., Marty, J.C., Flechtner, F., Balmino, G., Barthelmes, F., Biancale, R., 2014b. EIGEN-6C4 The latest combined global gravity field model including GOCE data up to degree and order 2190 of GFZ Potsdam and GRGS Toulouse. https://doi.org/10.5880/icgem.2015.1

Gardner, G.H.F., Gardner, L.W., Gregory, A.R., 1974. FORMATION VELOCITY AND DENSITY—THE DIAGNOSTIC BASICS FOR STRATIGRAPHIC TRAPS. GEOPHYSICS 39, 770–780. https://doi.org/10.1190/1.1440465

Gebrande, H., Castellarin, A., Lüschen, E., Millahn, K., Neubauer, F., Nicolich, R., 2006. TRANSALP—A transect through a young collisional orogen: Introduction. Tectonophysics, TRANSALP 414, 1–7. https://doi.org/10.1016/j.tecto.2005.10.030

Grad, M., Tiira, T., ESC Working Group, 2009. The Moho depth map of the European Plate. Geophysical Journal International 176, 279–292. https://doi.org/10.1111/j.1365-246X.2008.03919.x

Griffin, W.L., O'Reilly, S.Y., Afonso, J.C., Begg, G.C., 2009. The Composition and Evolution of Lithospheric Mantle: a Re-evaluation and its Tectonic Implications. J Petrology 50, 1185–1204. https://doi.org/10.1093/petrology/egn033

Grombein, T., Seitz, K., Heck, B., 2013. Optimized formulas for the gravitational field of a tesseroid. Journal of Geodesy 87, 645–660. https://doi.org/10.1007/s00190-013-0636-1

Heck, B., Seitz, K., 2007. A comparison of the tesseroid, prism and point-mass approaches for mass reductions in gravity field modelling. J Geod 81, 121–136. https://doi.org/10.1007/s00190-006-0094-0

Hirt, C., Rexer, M., 2015. Earth2014: 1 arc-min shape, topography, bedrock and ice-sheet models – Available as gridded data and degree-10,800 spherical harmonics. International Journal of Applied Earth Observation and Geoinformation 39, 103–112. https://doi.org/10.1016/j.jag.2015.03.001

Holland, T.J.B., Powell, R., 1998. An internally consistent thermodynamic data set for phases of petrological interest. Journal of Metamorphic Geology 16, 309–343. https://doi.org/10.1111/j.1525-1314.1998.00140.x

Kästle, E.D., El-Sharkawy, A., Boschi, L., Meier, T., Rosenberg, C., Bellahsen, N., Cristiano, L., Weidle, C., 2018. Surface Wave Tomography of the Alps Using Ambient-Noise and Earthquake Phase Velocity Measurements. Journal of Geophysical Research: Solid Earth 123, 1770–1792. https://doi.org/10.1002/2017JB014698

Kennett, B.L.N., Engdahl, E.R., Buland, R., 1995. Constraints on seismic velocities in the Earth from traveltimes. Geophysical Journal International 122, 108–124. https://doi.org/10.1111/j.1365-246X.1995.tb03540.x

Laske, G., Masters, G., Ma, Z., Pasyanos, M., 2013. Update on CRUST1.0 - A 1-degree Global Model of Earth's Crust. Presented at the EGU General Assembly 2013, 7-12 April, 2013, Vienna, Austria, Geophys Res Abstracts, pp. EGU2013-2658.

Macera, P., Gasperini, D., Ranalli, G., Mahatsente, R., 2008. Slab detachment and mantle plume upwelling in subduction zones: An example from the Italian South-Eastern Alps. Journal of Geodynamics 45, 32–48. https://doi.org/10.1016/j.jog.2007.03.004

Maddaloni, F., Pivetta, T., Braitenberg, C., 2020. Gravimetry and petrophysics for defining the intracratonic and rift basins of the western-central Africa zone,. Geophysics, under Review GEO-2019-0522.R1.

Mariani, P., Braitenberg, C., Ussami, N., 2013. Explaining the thick crust in Paraná basin, Brazil, with satellite GOCE gravity observations. Journal of South American Earth Sciences 45, 209–223. https://doi.org/10.1016/j.jsames.2013.03.008

Martin, S., Macera, P., 2014. Tertiary volcanism in the Italian Alps (Giudicarie fault zone, NE Italy): insight for double alpine magmatic arc. Italian Journal of Geosciences 133, 63–84. https://doi.org/10.3301/IJG.2013.14

Milani, L., Beccaluva, L., Coltorti, M., 1999. Petrogenesis and evolution of the Euganean Magmatic Complex, Veneto Region, North-East Italy. European Journal of Mineralogy 11, 379–400. https://doi.org/10.1127/ejm/11/2/0379

Mueller, S., Talwani, M., 1971. A crustal section across the Eastern Alps based on gravity and seismic refraction data. PAGEOPH 85, 226–239. https://doi.org/10.1007/BF00875411

Muttoni, G., Gaetani, M., Kent, D.V., Sciunnach, D., Berra, F., Garzanti, E., Mattei, M., Zanchi, A., 2009. Opening of the Neo-Tethys Ocean and the Pangea B to Pangea A transformation during the Permian. GeoArabia 14, 17–48.

Pavlis, N.K., Holmes, S.A., Kenyon, S.C., Factor, J.K., 2012. The development and evaluation of the Earth Gravitational Model 2008 (EGM2008). Journal of Geophysical Research: Solid Earth 117. https://doi.org/10.1029/2011JB008916

Pfiffner, A., 2015. Geologie der Alpen, Dritte Aufl. ed. Haupt Verlag.

Quick, J.E., Sinigoi, S., Mayer, A., 1995. Emplacement of mantle peridotite in the lower continental crust, Ivrea-Verbano zone, northwest Italy. Geology 23, 739–742. https://doi.org/10.1130/0091-7613(1995)023<0739:EOMPIT>2.3.CO;2

Quick, J.E., Sinigoi, S., Peressini, G., Demarchi, G., Wooden, J.L., Sbisà, A., 2009. Magmatic plumbing of a large Permian caldera exposed to a depth of 25 km. Geology 37, 603–606. https://doi.org/10.1130/G30003A.1

Rexer, M., Hirt, C., Claessens, S., Tenzer, R., 2016. Layer-Based Modelling of the Earth's Gravitational Potential up to 10-km Scale in Spherical Harmonics in Spherical and Ellipsoidal Approximation. Surv Geophys 37, 1035–1074. https://doi.org/10.1007/s10712-016-9382-2

Rottura, A., Bargossi, G.M., Caggianelli, A., Del Moro, A., Visonà, D., Tranne, C.A., 1998. Origin and significance of the Permian high-K calc-alkaline magmatism in the central-eastern Southern Alps, Italy. Lithos 45, 329–348. https://doi.org/10.1016/S0024-4937(98)00038-3

Scarascia, S., Cassinis, R., 1997. Crustal structures in the central-eastern Alpine sector: A revision of the available DSS data. Tectonophysics 271, 157–188. https://doi.org/10.1016/S0040-1951(96)00206-5

Schuster, R., Stüwe, K., 2008. Permian metamorphic event in the Alps. Geology 36, 603–606. https://doi.org/10.1130/G24703A.1

Sinigoi, S., Quick, J.E., Demarchi, G., Klötzli, U., 2011. The role of crustal fertility in the generation of large silicic magmatic systems triggered by intrusion of mantle magma in the deep crust. Contrib Mineral Petrol 162, 691–707. https://doi.org/10.1007/s00410-011-0619-2

Spada, M., Bianchi, I., Kissling, E., Agostinetti, N.P., Wiemer, S., 2013. Combining controlled-source seismology and receiver function information to derive 3-D moho topography for italy. Geophysical Journal International 194, 1050–1068. https://doi.org/10.1093/gji/ggt148

Spalla, M.I., Zanoni, D., Marotta, A.M., Rebay, G., Roda, M., Zucali, M., Gosso, G., 2014. The transition from Variscan collision to continental break-up in the Alps: insights from the comparison between natural data and numerical model predictions. Geological Society, London, Special Publications 405, 363. https://doi.org/10.1144/SP405.11

Spiess, R., Cesare, B., Mazzoli, C., Sassi, R., Sassi, F.P., 2010. The crystalline basement of the Adria microplate in the eastern Alps: a review of the palaeostructural evolution from the Neoproterozoic to the Cenozoic. RENDICONTI LINCEI 21, 31–50. https://doi.org/10.1007/s12210-010-0100-6

Spooner, C., Scheck-Wenderoth, M., Götze, H.-J., Ebbing, J., Hetényi, G., 2019. Density distribution across the Alpine lithosphere constrained by 3D gravity modelling and relation to seismicity and deformation. Solid Earth Discuss. 1–26. https://doi.org/10.5194/se-2019-115

Stampfli, G.M., Borel, G.D., 2002. A plate tectonic model for the Paleozoic and Mesozoic constrained by dynamic plate boundaries and restored synthetic oceanic isochrons. Earth and Planetary Science Letters 196, 17–33. https://doi.org/10.1016/S0012-821X(01)00588-X

Steinberger, B., Werner, S.C., Torsvik, T.H., 2010. Deep versus shallow origin of gravity anomalies, topography and volcanism on Earth, Venus and Mars. Icarus 207, 564–577. https://doi.org/10.1016/j.icarus.2009.12.025

Szwillus, W., Ebbing, J., Holzrichter, N., 2016. Importance of far-field topographic and isostatic corrections for regional density modelling. Geophys J Int 207, 274–287. https://doi.org/10.1093/gji/ggw270

Tenzer, R., Foroughi, I., Hirt, C., Novák, P., Pitoňák, M., 2019. How to Calculate Bouguer Gravity Data in Planetary Studies. Surveys in Geophysics 40, 107–132. https://doi.org/10.1007/s10712-018-9504-0

Tesauro, M., Kaban, M.K., Cloetingh, S.A.P.L., 2008. EuCRUST-07: A new reference model for the European crust. Geophysical Research Letters 35. https://doi.org/10.1029/2007GL032244

Torge, W., 2011. Geodesy, 3rd compl. rev. and extend. ed.. ed. De Gruyter, Berlin, Boston. https://doi.org/10.1515/9783110879957

Torge, W., Müller, J., 2012. Geodesy, 4th ed. ed. De Gruyter, Berlin, Boston. https://doi.org/10.1515/9783110250008

Uieda, L., Barbosa, V.C.F., Braitenberg, C., 2016. Tesseroids: Forward-modeling gravitational fields in spherical coordinates. GEOPHYSICS 81, F41–F48. https://doi.org/10.1190/geo2015-0204.1

Vaníček, P., Tenzer, R., Sjöberg, L.E., Martinec, Z., Featherstone, W.E., 2004. New views of the spherical Bouguer gravity anomaly. Geophysical Journal International 159, 460–472. https://doi.org/10.1111/j.1365-246X.2004.02435.x

Viganò, A., Scafidi, D., Martin, S., Spallarossa, D., 2013. Structure and properties of the Adriatic crust in the central-eastern Southern Alps (Italy) from local earthquake tomography. Terra Nova 25, 504–512. https://doi.org/10.1111/ter.12067

Wild-Pfeiffer, F., 2008. A comparison of different mass elements for use in gravity gradiometry. J Geod 82, 637–653. https://doi.org/10.1007/s00190-008-0219-8

Zampieri, D., 1995. Tertiary extension in the southern Trento Platform, Southern Alps, Italy. Tectonics 14, 645–657. https://doi.org/10.1029/94TC03093

Zanchetta, S., Garzanti, E., Doglioni, C., Zanchi, A., 2012. The Alps in the Cretaceous: a doubly vergent pre-collisional orogen: The Alps in the Cretaceous. Terra Nova 24, 351–356. https://doi.org/10.1111/j.1365-3121.2012.01071.x

Zanolla, C., Braitenberg, C., Ebbing, J., Bernabini, M., Bram, K., Gabriel, G., Götze, H.-J., Giammetti, S., Meurers, B., Nicolich, R., Palmieri, F., 2006. New gravity maps of the Eastern Alps and significance for the crustal structures. Tectonophysics 414, 127–143. https://doi.org/10.1016/j.tecto.2005.10.012
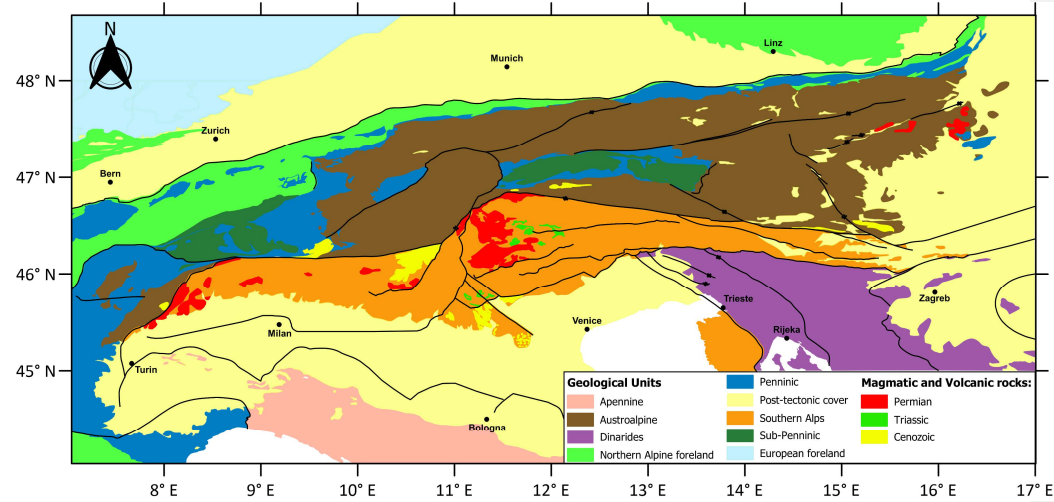
Figure 1 Geologic chart of the Alps modified after (Pfiffner, 2015) and main magmatic and volcanic bodies (Bigi et al., 1990a, 1990b; Schuster and Stüwe, 2008)

Formattato: Tipo di carattere: Grassetto, Non eseguire controllo ortografia o grammatica

Formattato: Tipo di carattere: Grassetto, Non eseguire controllo ortografia o grammatica
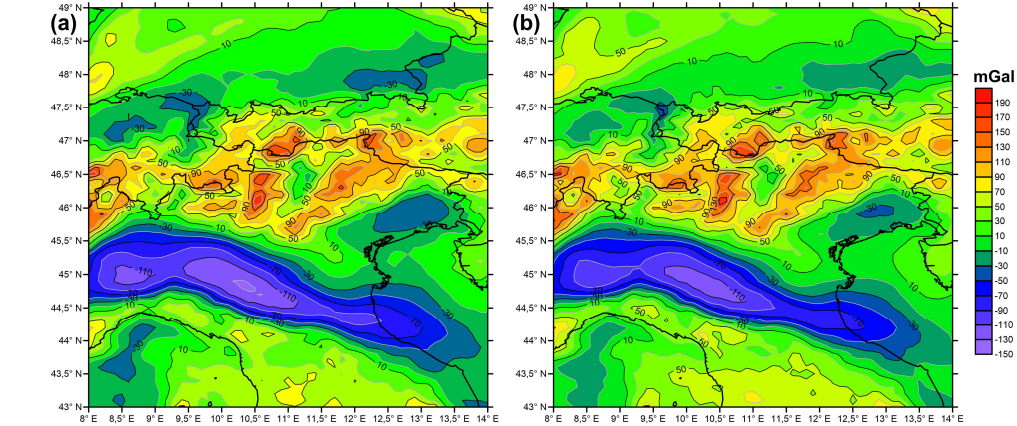
760   **Figure 2 – a) Gravity anomaly; b) Gravity disturbance; both functionals have been calculated with the gravity model EIGEN6c4 (Förste et al., 2014a); maximum degree N = 2190 and calculation height h = 5000 m.**

765
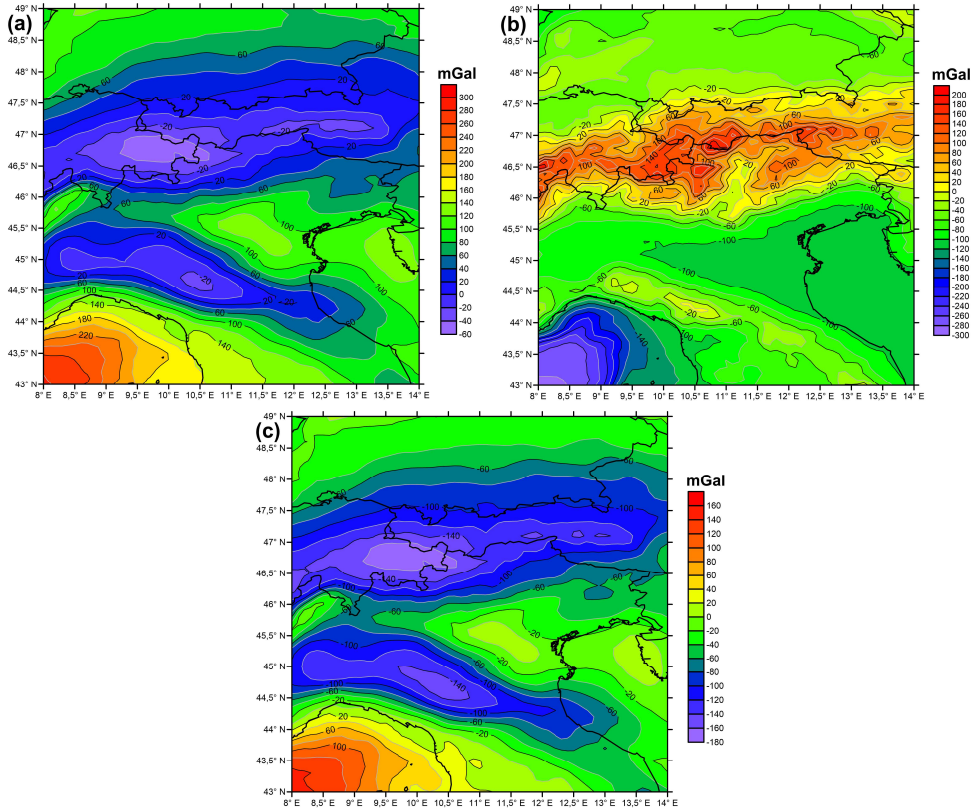
Figure 3 – a) Bouguer gravity disturbance, using gravity model EIGEN6c4 corrected with topography model RET2014 (N = 2190 and calculation height h = 5000m), b) Gravity disturbance of the model RET2014 (Rexer et al., 2016) (with N = 2190 and calculation height h = 5000m), c) Bouguer gravity disturbance, using gravity model EIGEN6c4 corrected with topography model TER2014 (both calculated with 10 < N ≤ 2190 and calculation height h = 5000m).

770

	Vs$_{min}$	Vs$_{max}$	Vs$_{mean}$	σ (std)	Vs$_{min}$ – σ	Vs$_{max}$ – σ
Crust1.0	3.650	4.685	4.069	0.173	3.896	4.242
EuCrust07	3.539	4.718	4.070	0.233	3.837	4.303
MohoGrad	3.524	4.725	4.110	0.209	3.901	4.318

Table 1 – Statistics of the S-wave velocity of tomographic model (Kästle et al., 2018), at the depths of Moho defined in three Moho models (Grad et al., 2009) MohoGrad, (Tesauro et al., 2008) EuCrust07 and (Laske et al., 2013) Crust1.0. Average value (Vsmean), Minimun value (Vsmin), Maximum value (Vsmax), σ (standard deviation) in km s⁻¹.

Formattato: Interlinea: 1,5 righe

775
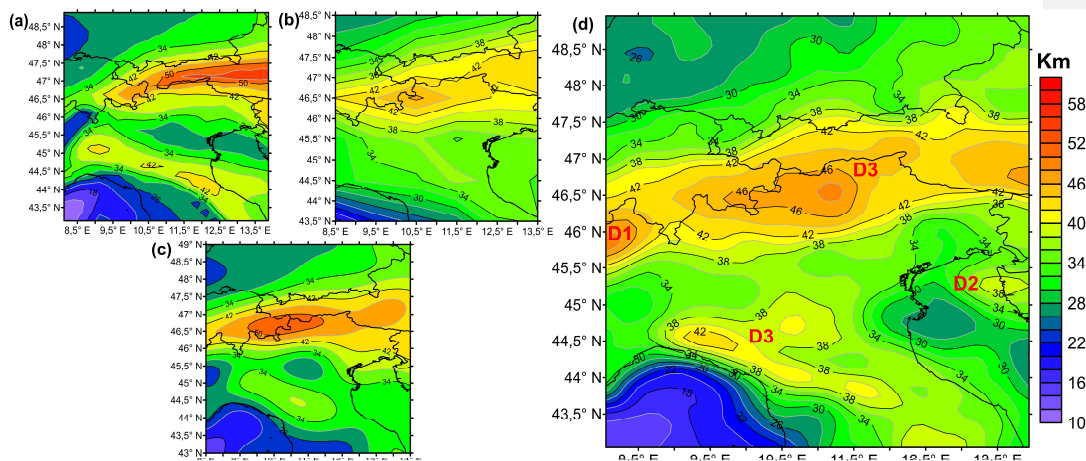
Figure 4 - Map of the Moho depth according to: a) EuCrust07 (Tesauro et al., 2008), b) CRUST1.0 (Laske et al., 2013), c) MohoGrad (Grad et al., 2009) and d)MohoTad (this work).

780
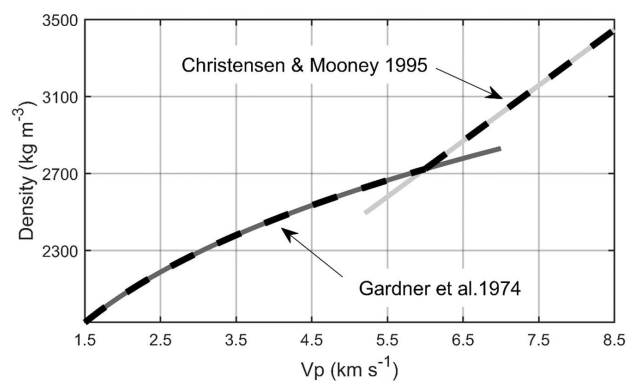
Figure 5 – Comparison of published densities versus Vp relations discussed in (Brocher, 2005), dark grey continuous line represents the Gardner's equation, light grey continuous line represents Christensen & Mooney linear regression fit, black dashed line represents the combined relation used in this work.
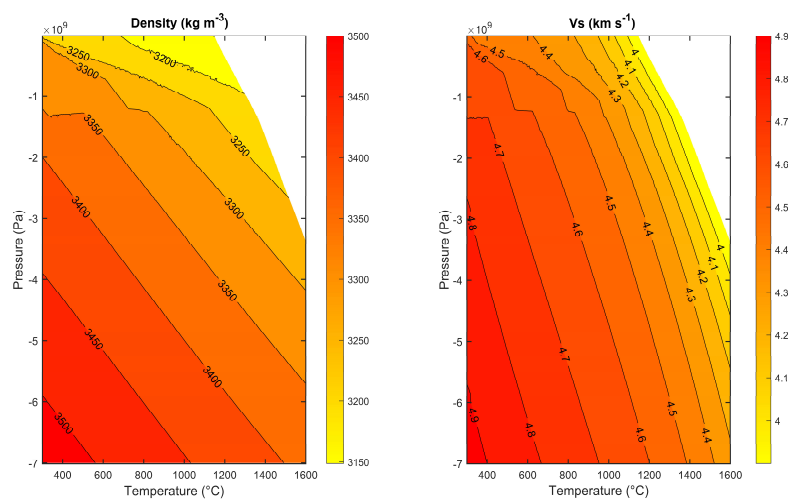
Figure 6 – Density and Vs plots of the model SUM as functions of pressure and temperature.
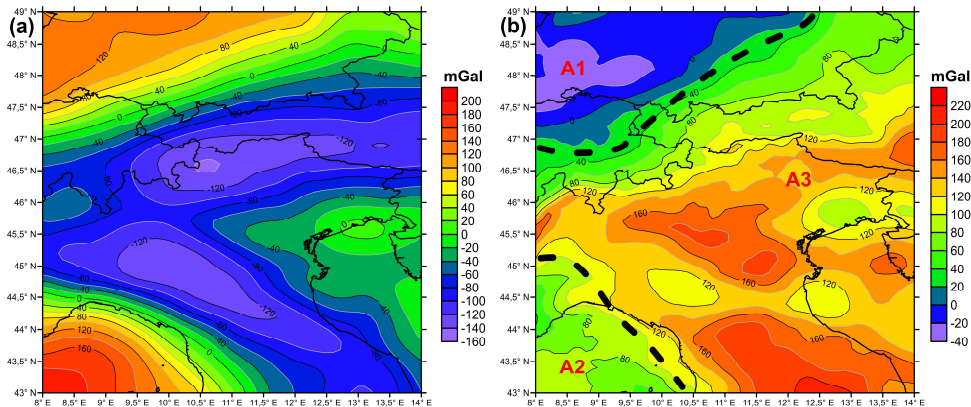
Figure 7 – a) Gravity anomaly map from the forward modelling, b) residual gravity map obtained from the difference between the Bouguer gravity disturbance (with 10 < N ≤ 2190) (Fig. 3c) and the forward gravity anomaly map. A1: Germany and Switzerland negative residual region; A2: positive residual region of Tyrrhenian basin; A3: Adriatic and Alpine domain characterized by high residual, black dashed lines divide the three different regions.

Eliminato: .

```
                    ┌──────────────────┐
                    │    RESIDUAL      │
                    │  GRAVITY MAP     │
                    └──────────────────┘
                             │
                    ┌──────────────────┐
                    │ 3° POLYNOMIAL FIT│
                    └──────────────────┘
                      │              │
        ┌────────────────────┐  ┌────────────────────┐
        │  MANTLE RESIDUAL   │  │  CRUSTAL RESIDUAL  │
        │    COMPONENT       │  │    COMPONENT       │
        │  (Long Periods)    │  │  (Short Periods)   │
        └────────────────────┘  └────────────────────┘
                 │                        │
        ┌────────────────────┐            │
   ┌──→ │  LINEAR INVERSION  │            │
   │    └────────────────────┘            │
   │             │                        │
   │    ┌────────────────────┐            │
   │    │ DENSITY CORRECTION │            │
   │    │ FORWARD MODELING   │            │
   │    └────────────────────┘            │
   │             │             ┌────────────────────┐
   │    ┌────────────────────┐ │  LINEAR ITERATIVE  │
   │    │  NEW RESIDUAL MAP  │ │     INVERSION      │
   │    └────────────────────┘ └────────────────────┘
   │  no         │ if                     │
   │    ┌────────────────────┐            │
   └────│   RMS < 3mGal      │            │
        └────────────────────┘            │
                 │ yes                    │
        ┌────────────────────┐            │
        │   NEW DENSITY      │←───────────┘
        │      MODEL         │
        └────────────────────┘
```
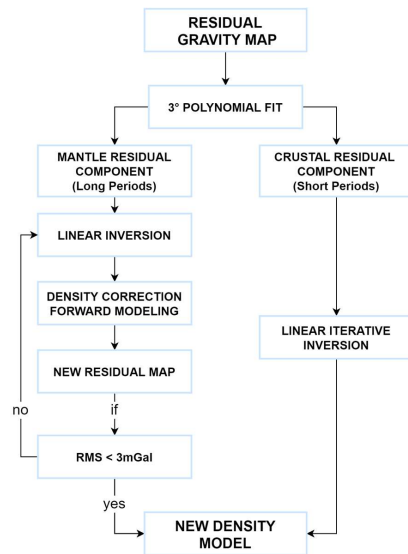
Figure 8 – Flowchart of the linear inversion algorithm
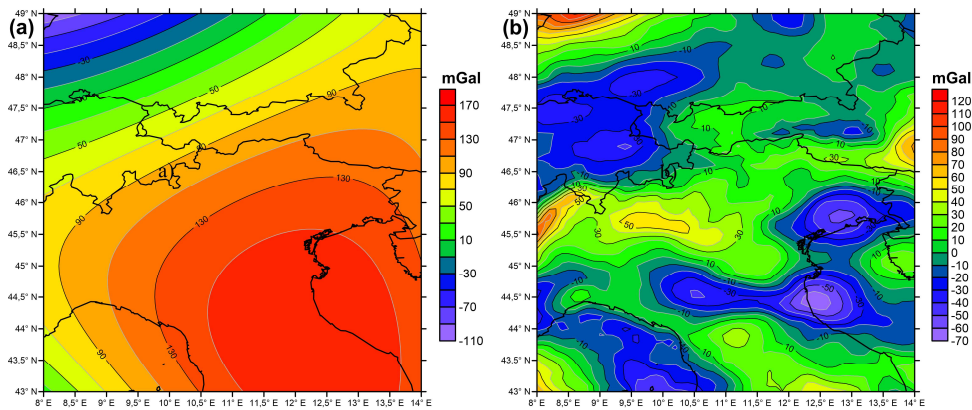
Figure 9 – a) Mantle residual component map (long-periods), b) Crustal residual component maps (short-periods)

800

805

810
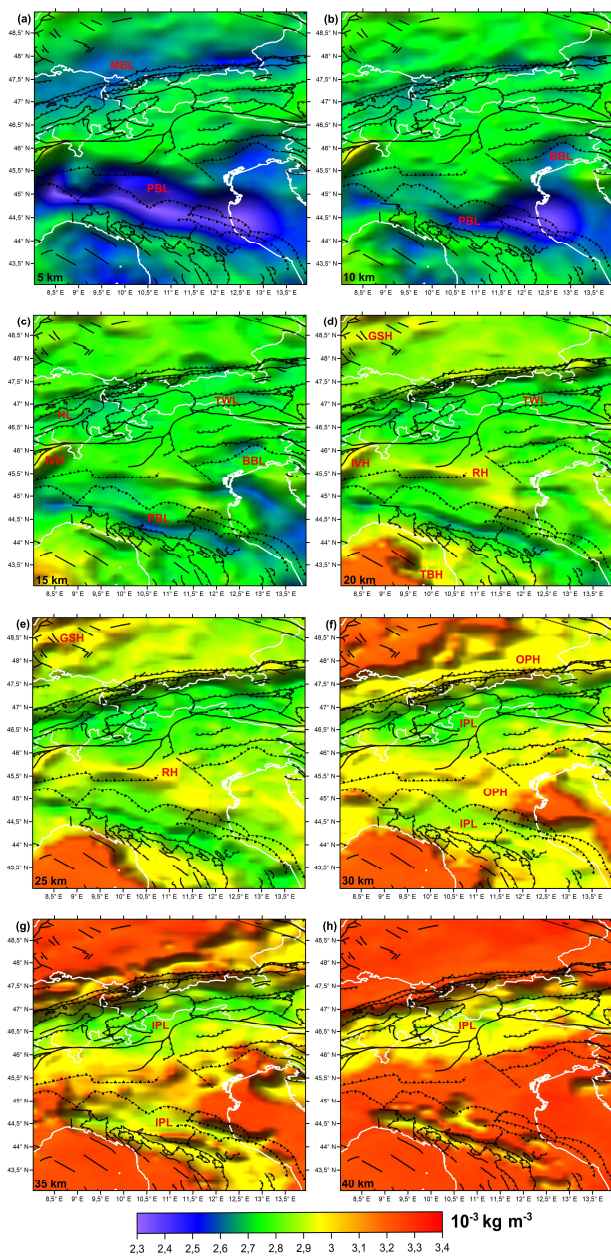
Figure 10 - Slice of density model, a)5km, b)10km, c)15km, d)20km, e)25km, f)30km, g)35km, h)40km. MBL: low density of Molasse basin; PBL: low density of Po basin; BBL: low density of Belluno basin; HL: low density of Helvetic nappe; TWL: low density of Tauern Window; IVH: high density of Ivrea-Verbano; GSH: high density of Rhine graben system; RH: high density values ridge; TBH: high density of Tyrrhenian basin; IPL: low density of orogen inner part; OPH: high density of orogen outer part.
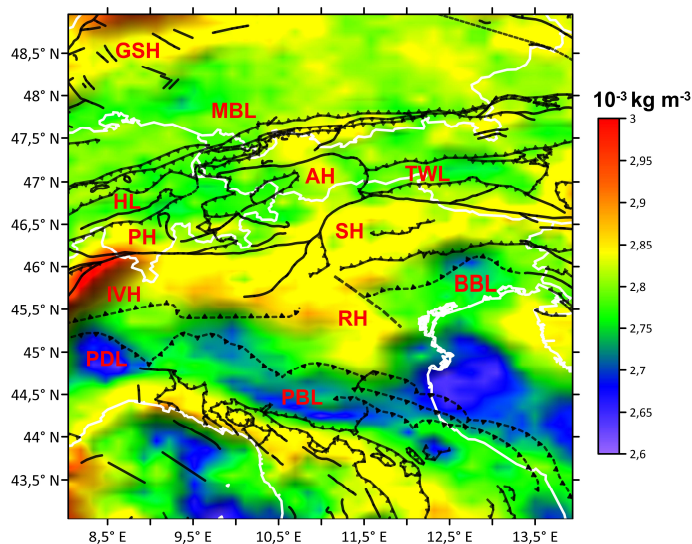
Figure 11 – Average density map; MBL: low density of Molasse basin; PBL: low density of Po basin; BBL: low density of Belluno basin; PDL: low density of Piedemont basin; HL: low density of Helvetic nappe ; PH: high density of Penninic Nappe; AH: high density of Austroalpine Nappe; TWL: low density of Tauern Window; IVH: high density of Ivrea-Verbano; GSH: high density of Rhine graben system; RH: high density values ridge

Eliminato: *<oggetto>*

Spostato in giù [1]: Figure 12 Sections across the 3D density model for illustration. A) A section oriented NW-SE centered on the Vicenza-Verona gravity high. B) SW-NE oriented profile centered on the gravity high. C) Detailed profile oriented WNW-SSE centered on the gravity high; MB1: first mushroom shaped body with high density; MB2: second mushroom shaped body; PB: Po basin; VVP: Venetian Volcanic Province; SGF: South Giudicarie fault; AB: Adamello Batholith; PL: Periadriatic Line; VTF: Valsugana Thrust Front; ATF: Apennine Thrust Front; RH: High density Ridge; IVH: High density anomaly of Ivrea-Verbano; BB: Belluno Basin; TP: Trento Platform; LB: Lombardian basin ¶
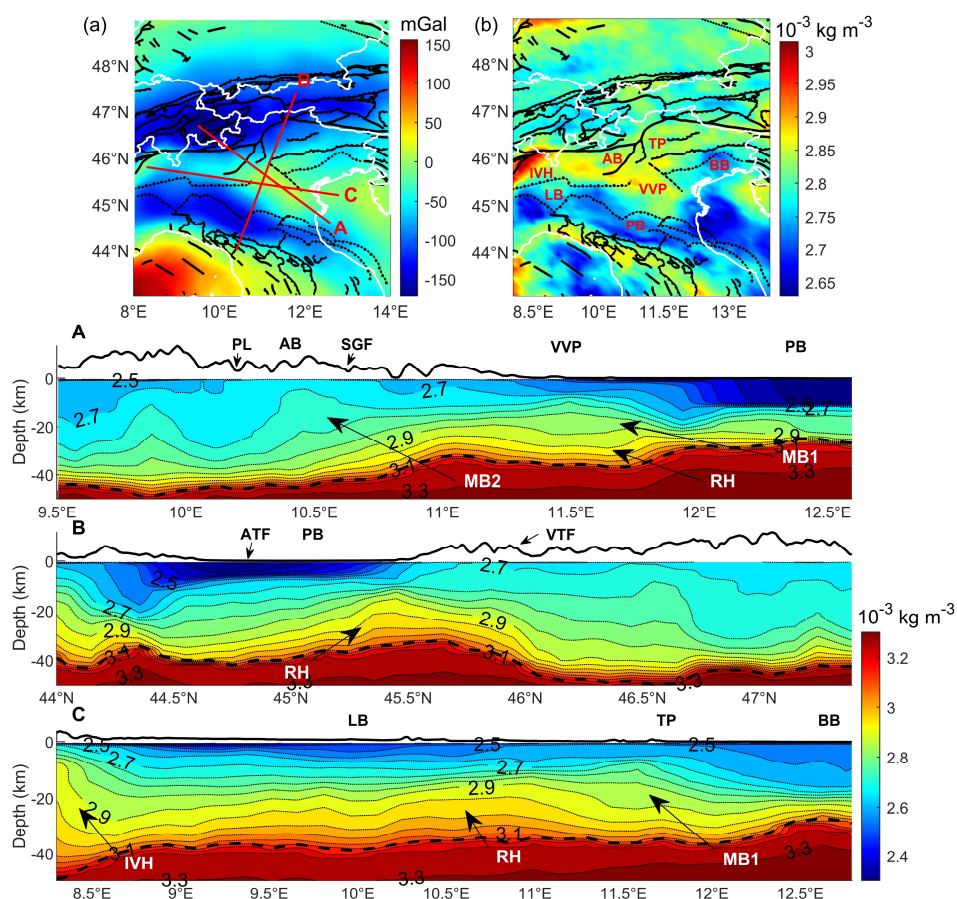
Figure 12 – a) Bouguer gravity disturbance (Fig. 3c), b) Average density map (Fig. 11). Sections across the 3D density model for illustration. A) A section oriented NW-SE centered on the Vicenza-Verona gravity high. B) SW-NE oriented profile centered on the gravity high. C) Detailed profile oriented WNW-SSE centered on the gravity high; MB1: first mushroom shaped body with high density; MB2: second mushroom shaped body; PB: Po basin; VVP: Venetian Volcanic Province; SGF: South Giudicarie fault; AB: Adamello Batholith; PL: Periadriatic Line; VTF: Valsugana Thrust Front; ATF: Apennine Thrust Front; RH: High density Ridge; IVH: High density anomaly of Ivrea-Verbano; BB: Belluno Basin; TP: Trento Platform; LB: Lombardian basin.

840